Polymer Nanowire/Fullerene Bulk Heterojunction Solar Cells: How Nanostructure Determines Photovoltaic Properties

Hao Xin,[†] Obadiah G. Reid,[‡] Guoqiang Ren,[†] Felix Sunjoo Kim,[†] David S. Ginger,[‡,*] and Samson A. Jenekhe[†,*]

[†]Department of Chemical Engineering and Department of Chemistry, University of Washington, Seattle, Washington 98195-1750 and [‡]Department of Chemistry, University of Washington, Seattle, Washington 98195

ABSTRACT We report studies of bulk heterojunction solar cells composed of self-assembled poly(3-butylthiophene) nanowires (P3BT-nw) as the donor component with a fullerene acceptor. We show that the nanostructure of these devices is the single most important variable determining their performance, and we use a combination of solvent and thermal annealing to control it. A combination of conductive and photoconductive atomic force microscopy provides direct connections between local nanostructure and overall device performance. Films with a dense random web of nanowires cause the fullerene to aggregate in the interstices, giving a quasi-ordered interpenetrating heterojunction with high short-circuit current density (10.58 mA/cm^2), but relatively low open circuit voltage (520 mV). Films with a low density of nanowires result in a random bulk heterojunction composed of small crystalline PCBM and P3BT phases. Fewer nanowires result in higher open circuit voltage (650 mV) but lower current density (6.02 mA/cm^2). An average power conversion efficiency of 3.35% was achieved in a structure which balances these factors, with intermediate nanowire density. The best photovoltaic performance would be realized in a material structure which maintains the interpenetrating network of nanowires and fullerene phases (high current density), but avoids the device bridging we observe, and the recombination and shunt losses associated with it (high open-circuit voltage).

KEYWORDS: polythiophene nanowires · bulk heterojunction solar cells · photoconductive nanocomposites · charge transport · conductive AFM · photoconductive AFM · photovoltaic properties

Polymer-based bulk heterojunction (BHJ) solar cells are a nascent technology that might provide low cost solar power conversion because of the low-cost high throughput manufacturing techniques which might be used in their production.[1−6] For several years, a composite of poly(3-hexylthiopehene) (P3HT) and phenyl-C61-butyric acid methyl ester (PCBM) has dominated research in this field, providing the highest certified efficiencies[7−11] until very recently. New polymers[12−25] have been synthesized and explored as the donor component in BHJ solar cells, and efficiency higher than 5% has been achieved in some of the narrow bandgap polymers.[17,18,21,26] The power conversion efficiencies commonly achieved in P3HT/PCBM bulk heterojunction solar cells have been up to 3−5%,[7−11,27,28] and the primary method of improving efficiency has been the optimization of the two-phase nanostructure of the donor and acceptor materials.[1−4,7,8,10,29−31] Various approaches[28,30−39] have been used to control the nanoscale film morphology of polymer-based bulk heterojunction solar cells, of which P3HT/PCBM is only one example. These methods include solution precipitation of P3HT nanofibers,[32] thermal annealing, pre- and postcathode deposition,[30] solvent annealing,[28,31,39] and the use of mixed solvents as a means to control aggregation of the polymer.[35,36,40−42]

We recently discovered that highly efficient BHJ solar cells can be made using pre-self-assembled[43] or *in situ*[44] self-assembled poly(3-butylthiophene) nanowires (P3BT-nw) as the donor component along with $PC_{61}BM$ or $PC_{71}BM$ as the acceptor. The chemical structures of P3BT and $PC_{71}BM$ are given in Scheme 1. These nanowires have a width of 10−15 nm (measured with TEM),[43,44] which is similar to a typical exciton diffusion length.[4] Moreover, the nanowires show high field-effect hole mobility in transistor geometry (8.0×10^{-3} cm^2/(V s)) in composite films with $PC_{61}BM$. These features suggest that P3BT nanowires might constitute an ideal donor component for BHJ solar cells. Indeed, in our preliminary work,[43] a power conversion efficiency (PCE) of 3.0% was obtained from the P3BT-nw/$PC_{71}BM$ composite, which is 1 order of magnitude higher than prior results from thermally induced phase-separated

*Address correspondence to jenekhe@u.washington.edu, ginger@chem.washington.edu.

Received for review October 26, 2009 and accepted March 04, 2010.

Published online March 11, 2010.
10.1021/nn9014906

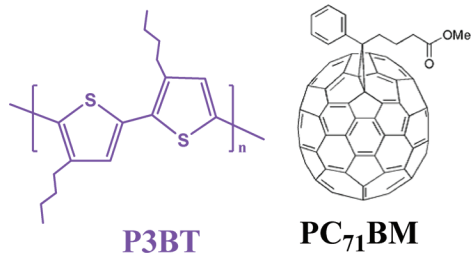

Scheme 1. Molecular structures of P3BT and $PC_{71}BM$.

P3BT:fullerene blend solar cells.[5,45] However, the device structure was never fully optimized or characterized.

In this paper, we systematically vary the morphology of P3BT-nw/fullerene composites through a combination of solvent and thermal annealing. The photovoltaic performance of the composite material varies dramatically with the induced structural variations, and we use a combination of bulk charge transport, conductive/photoconductive atomic force microscopy (cAFM/pcAFM),[46−49] transmission electron microscopy (TEM), and X-ray/electron diffraction data to explain how the local film morphology changes the bulk device performance. A homogeneous dispersion of fullerene in the P3BT-nw matrix in unannealed devices showed poor photovoltaic performance, with low open-circuit voltage and short circuit current. Thermal annealing of a well-dried stable film caused aggregation of fullerene in the interstitial spaces of the nanowire network and dramatically improved both the short-circuit current and open-circuit voltage of the device. When the film was annealed before drying was complete, the P3BT nanowires were partially dissolved, resulting in a much lower current density but improved open circuit voltage.

RESULTS AND DISCUSSION

Figure 1 shows the current density−voltage curves of the P3BT-nw/$PC_{71}BM$ blend solar cells under simulated (AM 1.5) solar illumination. The data set includes two different compositions of 1:0.5 and 1:1 P3BT/$PC_{71}BM$, each prepared under four different drying and annealing conditions. Table 1 shows the processing

TABLE 1. Film Processing Conditions Used in This Study

condition	A	B	C	D
aging time (min)	3	35−50[a]	100	100
annealing (175 °C, 10 min)	yes	yes	yes	no

[a]Time at which film color changed from orange to purple, about 50, 45, and 35 min, respectively, for pure P3BT-nw, P3BT-nw:$PC_{71}BM$ (1:0.5), and P3BT-nw:$PC_{71}BM$ (1:1) films.

conditions used to vary the blend morphology, each of which will henceforth be referred to by the name listed in the table (*e.g.*, condition A corresponds to a 3 min drying time before a 10 min thermal annealing step). The photovoltaic parameters derived from these *J*—*V* curves, the short-circuit current density (J_{sc}), the open circuit voltage (V_{oc}), the fill factor (FF), and the power conversion efficiency (PCE), are plotted in Figure 2a−d, and the full collection of numerical data can be found in Table 2, together with the series and parallel resistance deduced by the inverse gradient of the *J*—*V* curves.[50] The absorption spectra of the solar cells in Figure 1 and the average external quantum efficiency spectra of some of the devices are given in the Supporting Information (Figure S1). Figure 2e shows the hole mobility in each blend, including pure P3BT-nw films, as a function of processing condition, measured *via* the space−charge limited current method. These values are also collected in Table 2. The dark *J*—*V* curves of the hole-only devices and fits using the Mott-Gurney law are available as Supporting Information (Figure S2).

The strong dependence of the power conversion efficiency on processing conditions and composition is evident in Figure 2a. For the 1:0.5 P3BT-nw/$PC_{71}BM$ blend composition, the best average performance was achieved in the device dried for 15 min before annealing (condition A*) with an average PCE of 3.4%, while for the 1:1 composition, the highest PCE (2.9%) was obtained in devices dried for 100 min before annealing (condition C). We note that a PCE of 3.6% was observed in a P3BT-nw/$PC_{71}BM$ (1:0.5) blend device processed under condition A when a higher molecular weight (as judged by its low solubility) P3BT sample was used, in-

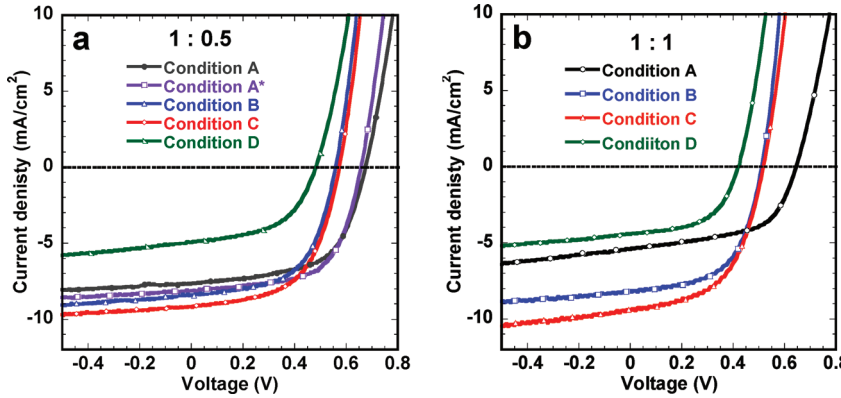

Figure 1. The *J*−*V* characteristics of P3BT-nw:$PC_{71}BM$ solar cells with a structure of ITO/PEDOT/P3BT-nw:$PC_{71}BM$/LiF/Al at blend ratio of 1:0.5 (a) and 1:1 (b). The curves were measured under AM1.5 white light illumination at 100 mW/cm^2.

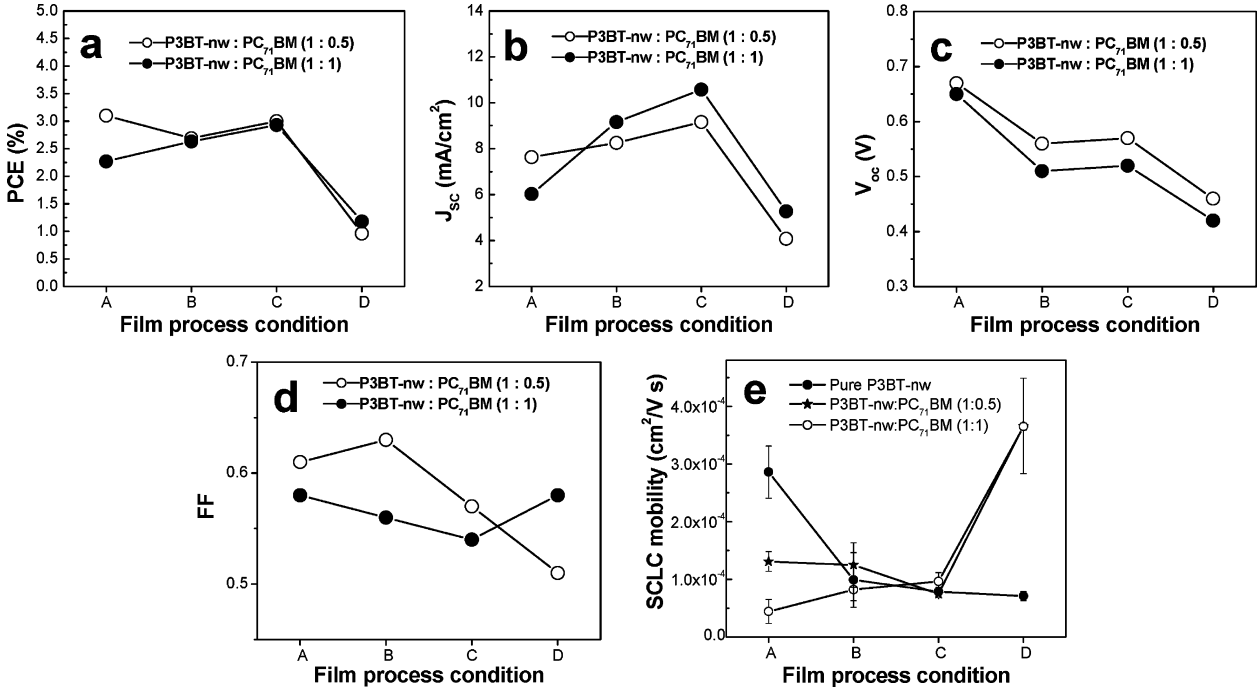

Figure 2. The photovoltaic parameters of the P3BT-nw/$PC_{71}BM$ solar cells with the composition of 1:0.5 and 1:1 and the SCLC hole mobilities of P3BT-nw and P3BT-nw/$PC_{71}BM$ blend films as a function of the processing condition: (a) PCE; (b) J_{sc}; (c) V_{oc}; (d) FF; and (e) SCLC.

dicating dependence of the performance of the P3BT-nw/fullerene solar cells on molecular weight. In both blend compositions, the unannealed samples performed the worst and improved dramatically when annealed. Figure 2 panels b−d show the variation in J_{SC}, V_{OC}, and FF with processing conditions. The trends in J_{SC} and V_{OC} are opposing, both with blend composition and processing conditions. The V_{OC} is generally higher for the 1:0.5 P3BT-nw/$PC_{71}BM$ blend than for the 1:1 blend composition, but J_{SC} is lower for the 1:0.5 blend than for the 1:1 blend. Likewise, V_{OC} decreases with increasing drying time, while J_{SC} increases. However, both J_{SC} and V_{OC} reach their minimum in the devices which were not thermally annealed (condition D). The highest occupied molecular orbital (HOMO) level of the P3BT nanowires measured from the onset of the electrochemical oxidation peak is −4.6 eV and the lowest unoccupied molecular orbital (LUMO) is estimated to be −2.75 eV by using the optical band gap of P3BT nanowire [LUMO level = HOMO level + E_g^{opt} = −4.6 + 1.85 eV[41]]. This HOMO energy level determined from electrochemistry is in excellent agreement with −4.57 eV measured by photoemission spectroscopy for P3HT which has an identical backbone as P3BT.[51]

The space-charge limited current (SCLC) hole mobility only varies by a factor of ~5 across all blend compositions and processing conditions (Figure 2e). Nevertheless, some puzzling trends are apparent. First, pure nanowire films show the highest hole mobility with the shortest drying time (condition A), while the blend films reach a roughly equivalent maximum in their unannealed state (condition D). Second for the blend films processed under condition C (long drying time), where the short circuit current is maximized and the power conversion efficiency is quite high, the SCLC hole mobility is relatively low. Finally, the blend films processed under condition D (not annealed) have the highest SCLC hole mobility, but also the lowest photovoltaic performance.

TABLE 2. Summary of the Photovoltaic Properties of P3BT-nw/$PC_{71}BM$ Solar Cells[a]

P3BT-nw:$PC_{71}BM$	condition	SCLC-hole ($cm^2/(V\,s)$)	R_s ($\Omega\,cm^2$)	R_p ($\Omega\,cm^2$)	I_{sc} (mA/cm^2)	V_{oc} (V)	FF	PCE (%)
1:0.5	A	1.31×10^{-4}	14.3	652	7.63	0.67	0.61	3.10
1:0.5	A[b]	1.42×10^{-4}	11.2	750	8.12	0.66	0.63	3.35
1:0.5	B	1.25×10^{-4}	10.7	560	8.25	0.56	0.58	2.69
1:0.5	C	4.74×10^{-5}	11.1	372	9.16	0.57	0.57	3.00
1:0.5	D	3.66×10^{-4}	20.2	510	4.07	0.46	0.51	0.96
1:1	A	4.43×10^{-5}	13.4	740	6.02	0.65	0.58	2.27
1:1	B	8.20×10^{-5}	11.1	556	9.16	0.51	0.56	2.63
1:1	C	9.62×10^{-5}	11.2	367	10.58	0.52	0.54	2.93
1:1	D	3.65×10^{-4}	37.9	505	5.27	0.42	0.58	1.18

[a]Average of at least 5 devices. [b]Annealed after 15 min aging.

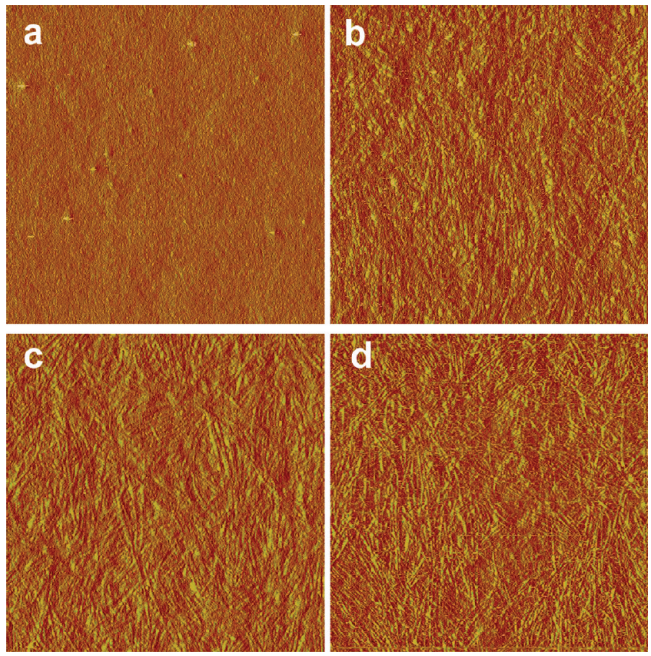

Figure 3. Tapping mode AFM phase images of P3BT-nw/$PC_{71}BM$ (1:1) blend films prepared under condition A (a), condition B (b), condition C (c), and condition D (d). The dimension of the images is 5 × 5 μm^2.

This variation in the photovoltaic performance and charge carrier mobility of the blend with the processing parameters is an expected, well established, feature of excitonic bulk-heterojunction solar cells. The questions we must answer are what are the changes in morphology that lead to these variations in performance? and can we explain why a particular change in nanostructure changes the bulk performance parameters in the way we observe? We answer these questions in two ways. First, we apply standard nanoscale characterization tools, AFM, TEM, and XRD, to investigate the nanostructure of these materials, and how it changes with processing conditions. Second, we apply a combination of conductive and photoconductive AFM (cAFM and pcAFM) measurements to directly measure how these changes in nanostructure effect charge transport and short-circuit photocurrent at the nanoscale. We focus only on the 1:1 blend for this detailed structural characterization because it exhibits the highest short circuit current density, greatest variation in performance with different processing conditions, and greater reproducibility in our pcAFM measurements than the 1:0.5 blends. In addition, since the trends in photovoltaic parameters in both blend systems are very similar, we expect the structure−property relationships we establish in one blend system to transfer to the other.

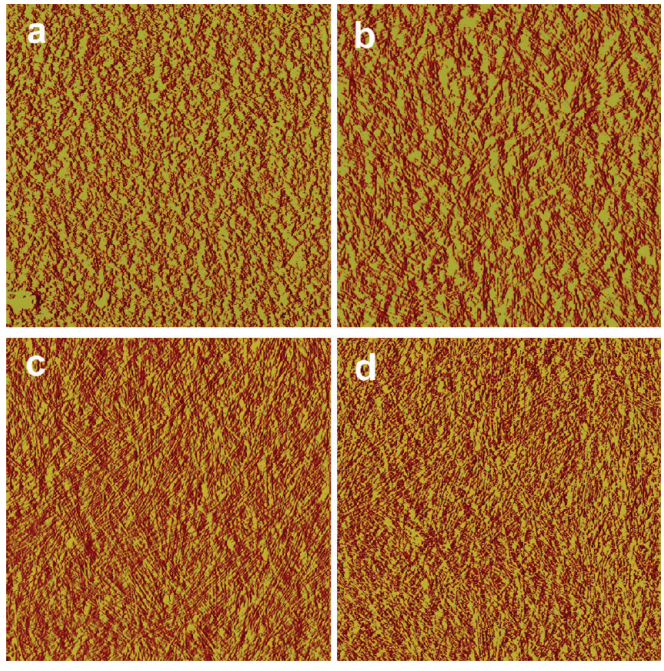

Figure 4. Tapping mode AFM phase images of P3BT-nw films prepared under the four different conditions in Table 1. (a) condition A; (b) condition B; (c) condition C; (d) condition D. The dimension is 5 × 5 μm^2 and the scale is 30° for all the images.

Figure 3 panels a−d show AFM phase images of the 1:1 P3BT-nw/$PC_{71}BM$ blend, prepared using each of the four different processing conditions. Interpretation of these images is best made with a direct comparison to the analogous structural evolution of films composed purely of P3BT nanowires. Figure 4a−d shows an equivalent data set of AFM phase images of pure P3BT-nw films, prepared using the same four processing conditions.

We discuss the images in order of decreasing drying time. The phase images of films treated with condition D (not annealed, Figures 3d and 4d) both show P3BT nanowires distributed in a random network. The main distinction is that the nanowire features in the blend film (Figure 3d) are thicker than those in the pure nanowire film (Figure 4d). After the film undergoes thermal annealing (condition C, Figures 3c and 4c), we see no reduction in the density of nanowires within the films, but those in the blend widen further, while those in the pure nanowire film remain unchanged. There is also a slight increase in the order of both films, with the nanowires tending to straighten and align parallel to one another. When the drying time is shortened to ~35 min (condition B), no further widening of the nanowire features is observed in the blend, but the nanowires in both the blend and pure nanowire films begin to disappear. In the pure nanowire film, the disappearance of the nanowires is accompanied by the growth of ~50 nm domains which appear featureless in the phase image. When the drying time is reduced to only 3 min (condition A), very few if any nanowires are observed in either blend. The pure nanowire film shows a random arrangement of distinct ~50 nm domains, while the blend film appears very homogeneous.

The three prominent features we have observed are (1) widening of nanowire structures in the blend films compared to the pure nanowires, and further widening upon initial annealing; (2) dissolution of the

nanowires when films are annealed after short drying times; and (3) formation of relatively large, distinct domains in the pure nanowire films, and an amorphous structure in the blend films, as the nanowires disappear. We propose the following explanations of these observations. First, we hypothesize that the apparent widening of the nanowires in the blend film is due to aggregation of fullerene molecules in the interstices of the P3BT-nw structure, or possibly a preferential aggregation of fullerene along the nanowires. We attribute the further widening observed upon subsequent annealing at long drying times (condition C) to crystallization of the fullerene and further aggregation between the polymer wires. Second, we believe that the shortening and disappearance of nanowires when the drying time is decreased is due to the residual solvent in the films. When the nanowires are heated in the presence of sufficient solvent, they dissolve into their constituent molecules. Third, we hypothesize that the formation of large distinct phases in the pure P3BT films as the nanowires disappear is evidence for the formation of a bulk crystalline phase. The lack of such a phase in the blend film can be explained if the presence of the fullerene molecules inhibits the crystallization of the polymer.

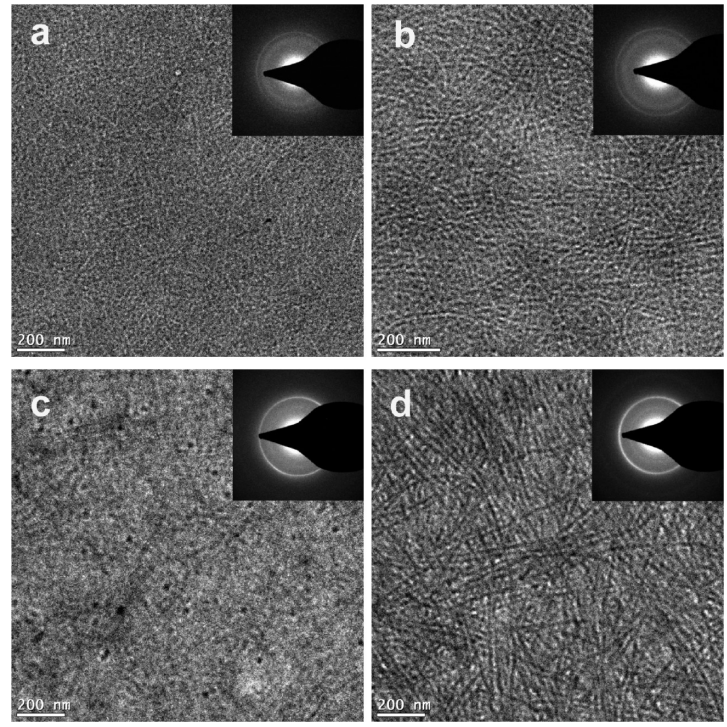

Figure 5. Bright-field TEM images of P3BT-nw/$PC_{71}BM$ (1:1) blend thin films (a, b) and pure P3BT-nw films (c, d) under condition A (a, c) and condition D (b, d). The films were spin-casted on top of ITO/PEDOT substrates and peeled off by putting the samples in water. The insets are the electron diffraction of the corresponding film.

The second of these three hypotheses is straightforward. However, the other two merit further investigation. We use TEM and XRD to help test these hypotheses, providing more detailed structural information, including the crystallinity of the polymer and fullerene phases.

Bright-field TEM images and the associated electron diffraction patterns for both the 1:1 P3BT-nw/$PC_{71}BM$ blend, and the pure nanowire films are shown in Figure 5a−d. Figure 5 panels a and b show the 1:1 blend film prepared with condition A (short drying time), and condition D (long drying time), respectively. Figure 5 panels c and d show the pure P3BT-nw films prepared in the same way as the blend. Like the AFM phase images, these reveal some significant differences in the blend film compared to the pure P3BT nanowires. For the samples which were fully dried before annealing, (Figure 5b,d) the interconnected P3BT nanowire network is apparent in both samples, but there is a distinct difference between the structure of the pure nanowire film (Figure 5d) and the blend (Figure 5b). The weblike pattern of crossing nanowires in Figure 5d is altered in Figure 5b by an irregular widening of the nanowires. For the samples that were dried for only a short time before annealing (Figure 5a,c) there are very few, if any, nanowires evident in either the blend (Figure 5a) or the pure polymer film (Figure 5c). However, again there is a distinct difference between the two. While the blend film is homogeneous (Figure 5a), the pure nanowire film exhibits a random distribution of distinct dark domains (Figure 5c).

In both the blend and pure polymer films, there are three strong electron diffraction rings (Figure 5, inset) associated with crystalline P3BT at q of 0.8, 0.16, and 2.6 nm^{-1}, corresponding to the (100), (200), and (010) diffractions,[52,53] respectively. In addition to the P3BT signal, the electron diffraction for the blend films show a ring at 2.2 nm^{-1} (d = 0.46 nm) due to $PC_{71}BM$ crystals.[9]

It was expected that the electron diffraction signal associated with the crystalline polymer phase would be less intense when the density of polymer nanowires is low (Figure 5a,c). However, the remaining strength of this signal, even when there are very few or no nanowires visible in the TEM image, is strong evidence for the formation of a bulk crystalline phase, and we see that this behavior (strong diffraction without visible nanowires) is much more pronounced in the pure polymer film than in the blend.

This data is consistent with our AFM results and supports our previous interpretation. The TEM images show an alteration in the morphology of the nanowires in the blend film compared with the pure polymer nanowire film, which we interpret as evidence for aggregation of fullerene in between and/or along the nanowires. The electron diffraction data also support our hypothesis that the pure polymer films form a bulk crystalline phase upon dissolution of the nanowires and

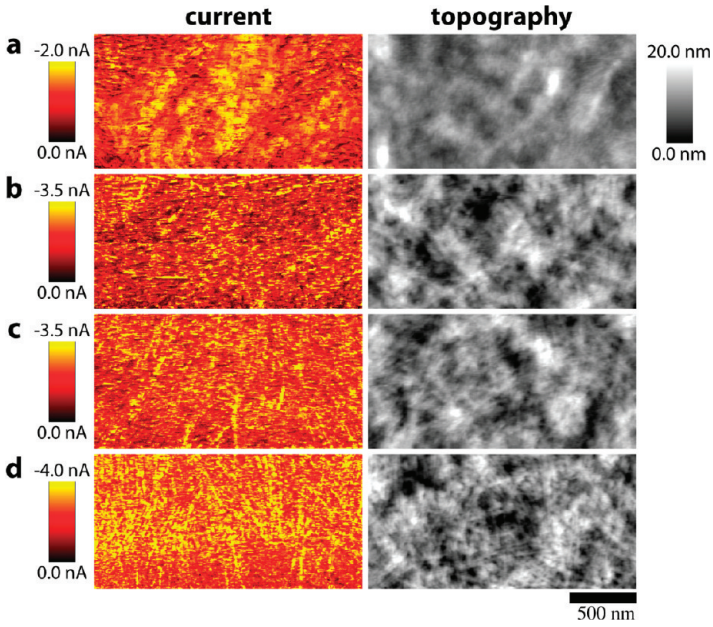

Figure 6. Conductive AFM images of pure P3BT-nw films processed under condition A (a), condition B (b), condition C (c), and condition D (d). A +3 V tip bias was used for all images.

that the presence of fullerene in the blend inhibits this polymer crystallization.

Further evidence for the formation of a bulk P3BT crystal phase comes from XRD measurements. A distinct shift in the d-spacing of the (100) polymer diffraction from ~1.25 to 1.31 nm is observed when the nanowires are dissolved *in situ*, indicating a change in crystal structure. Full XRD spectra can be found in Supporting Information (Figure S3).

Thus far, we have built a detailed picture how a combination of solvent and thermal annealing affects the nanostructure of P3BT-nw/$PC_{71}BM$ composites and shown how the bulk performance varies between these different nanostructures. However, it is difficult with these traditional nanoscale characterization techniques (AFM, TEM, and XRD) to draw firm conclusions about why one film structure is better for photovoltaic performance and/or charge transport than another, and thus how to improve performance in the future. We use a combination of conductive- and photoconductive-AFM (cAFM and pcAFM) to bridge this gap, and provide direct local correlations between device performance and the nanostructure of the film. The hole-only cAFM images give us information on the hole transport network, whereas the pcAFM data give us maps of local short-circuit photocurrent as discussed below. Further explanation of how we interpret the results of each of these experiments is given in the Supporting Information Figure S7.

Figure 6a–d shows a set of cAFM images including topography (right) and current (left) images of pure P3BT-nw films prepared under the four drying and annealing conditions. The images show the hole-only transport properties of the films with the tip injection holes,[47] since we use gold-coated AFM tips and a negative substrate bias. The trend with drying time is clear, both in the topography and current images. As the drying time decreases (bottom to top), the nanowires disappear from the film structure until we are left with very few, or no intact nanowires, and features consistent with small bulk crystalline phases (higher current regions, Figure 6a) appear. The nanowires visible clearly in Figure 6d,c exhibit current densities at least a factor of 2 higher than the surrounding film structure, demonstrating enhanced charge transport along the wires.

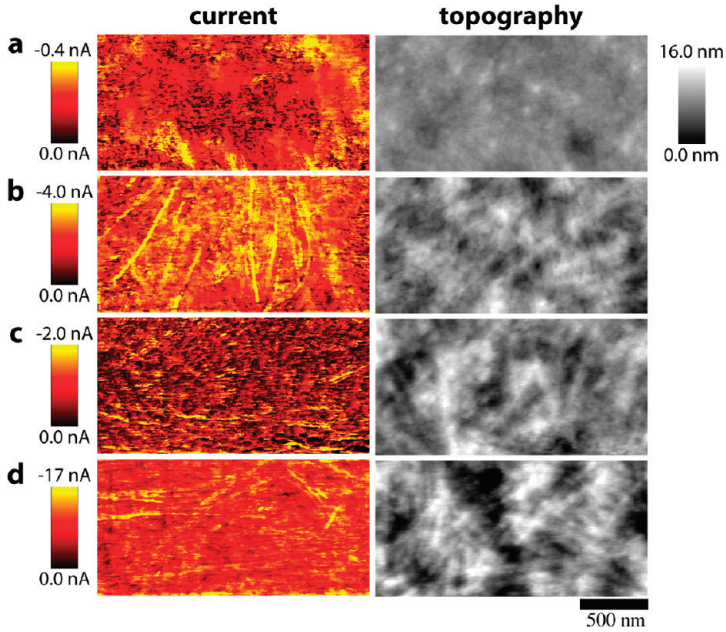

Figure 7. Conductive AFM images of P3BT-nw:$PC_{71}BM$ (1:1) films processed under condition A (a), condition B (b), condition C (c), and condition D (d). A +3 V tip bias was used for all images.

Figure 7 shows a set of cAFM images, including topography (right) and current (left) for 1:1 P3BT-nw:$PC_{71}BM$ blend films processed under the four different drying and annealing conditions. Examination of the topography images (right) shows the same trend in nanowire structure that we observed for the pure P3BT-nw films: as drying time decreases (bottom to top), the nanowires begin to disappear. However, we also observe some significant differences: the nanowires appear much wider in the blend film, and present an irregular appearance in topography, as observed in the previous TEM and AFM phase images. We discuss the current images one by one, in order of decreasing drying time.

For the film prepared under condition D (not annealed; Figure 7d), the current image shows far fewer "hot" nanowires that are carrying double the background current, and those only appear on the surface over a short distance, as compared to the pure nanowire film (Figure 6d).

For the blend film processed under condition C (long drying time; Figure 7c), there is more evidence in the current image of nanowires extending significant distances along the surface of the film. However, we see that most of the nanowires are now transporting *less* current than the background, while a few others remain bright, with significantly more current. This observation suggests aggregation of the fullerene phase between and/or along/over the polymer nanowires. As with our experiments on the pure P3BT-nw films, the work function of our tip and substrate and the negative tip bias we use imply that our c-AFM images provide a map of the hole-only transport properties of the films. Thus, we infer that distinct dark spots in the current image correspond to fullerene-rich phases near the surface of the film that prevent efficient hole injection.

For the film processed under condition B (intermediate drying time, Figure 7b), the current image shows many more nanowires, well aligned with one another, and parallel to the film surface, although the total number of wires evident in the topography is reduced. Nearly all of these wires again show the enhancement in current relative to the background. From this we infer that when the sample is annealed in the presence of a greater residual concentration of solvent, and the nanowires have more freedom to reorganize and/or dissolve, fullerene aggregation is no longer constrained to the volume between the nanowires and forms a more random array of nanocrystals, similar to the structure in traditional polymer/fullerene BHJ films.[5,8,28,54] Dark patches indicate the remaining presence of fullerene phases on the surface, but they appear less organized, and not clearly associated with the nanowires.

Finally, for the film processed under condition A (short drying time; Figure 7a), we see almost no remaining nanowires in either the topography or the current images. Furthermore there is significantly less evidence of bulk crystalline P3BT phases, relative to the pure polymer film (Figure 6a), although there are some large amorphous bright (high current) shapes which may indicate more crystalline, or better vertically interconnected regions of the P3BT film. Additionally we see an extensive disordered array of small dark spots which may be fullerene nanocrystals on the surface.

Taking all of this data together, we can draw three specific conclusions that help explain the bulk charge transport properties of these composites in terms of the nanostructure of the films. First, we concluded from our structural characterization that the polymer nanowire density decreases with decreasing drying time prior to annealing. Films processed under condition A contain almost no nanowires, while those processed under condition D contain many. We have also shown qualitatively through our cAFM results that the nanowires have a significantly enhanced hole transport properties relative to the bulk of the film. Why then, does the pure polymer film with the most nanowires have the lowest bulk SCLC hole mobility, and that with the fewest nanowires have the highest? And, why does the 1:1 P3BT-nw/$PC_{71}BM$ blend show exactly the opposite trend?

We propose that the answer is in the alignment of the nanowires in the film. All of our microscopy techniques show that, in the pure polymer films, the P3BT nanowires are aligned in the plane of the film. Our cAFM images in particular show nanowires extending lengthwise across the surface for multiple micrometers in the pure P3BT-nw film processed under condition D (Figure 6d). Thus we expect an anisotropy in the bulk hole mobility of the film. The enhanced longitudinal hole mobility of the nanowires does not translate into an especially high SCLC mobility because the wires are oriented perpendicular to the direction of charge transport. However, upon annealing after a short drying time, bulk crystalline phases of P3BT form as the nanowires dissolve, and these structures provide increased vertical hole mobility. To test this hypothesis we used field effect transistors to measure the horizontal hole mobility of these films. The results from these measurements show just what we would expect, with the highest hole mobility ($\sim 5 \times 10^{-3}$ $cm^2/(V\ s)$) in pure P3BT films which have a high density of nanowires and the lowest mobility ($\sim 3.5 \times 10^{-3}$ $cm^2/(V\ s)$) in those which lack them. The complete results of these measurements appear in the Supporting Information (Figures S4 and S5).

This description accounts very well for the trend in bulk SCLC hole mobility in the pure P3BT-nw films, but it does not yet explain the high hole mobility of blend films prepared under condition D (not annealed) compared with pure P3BT-nw films prepared under the same processing conditions. Again, the answer lies in the orientation of the nanowires. In examining Figure 7d we noted a significant difference between it and 6d. The cAFM image of the blend film does not show long sections of polymer nanowires extending horizontally across the surface. Instead we see relatively short sections, on the order of 0.5 μm in length, despite the fact that TEM and AFM topography images show a high density of nanowires with lengths of several micrometers. We suggest that this difference in the surface morphology may be due to a different organization of the nanowires in the film. Rather than lying in horizontal mats, the additional volume of fullerene in the film structure may allow the wires to assume a somewhat more isotropic, randomly distributed 3D structure, in which more of the wires penetrate vertically through the film, enhancing the bulk hole mobility. When the blend films are annealed (Figure 7b,c), we again see nanowires which are oriented horizontally along the surface of the film for long distances, and the bulk SCLC hole mobility drops.

Finally, we address the nanoscale variations in photovoltaic performance, and how they relate to the film

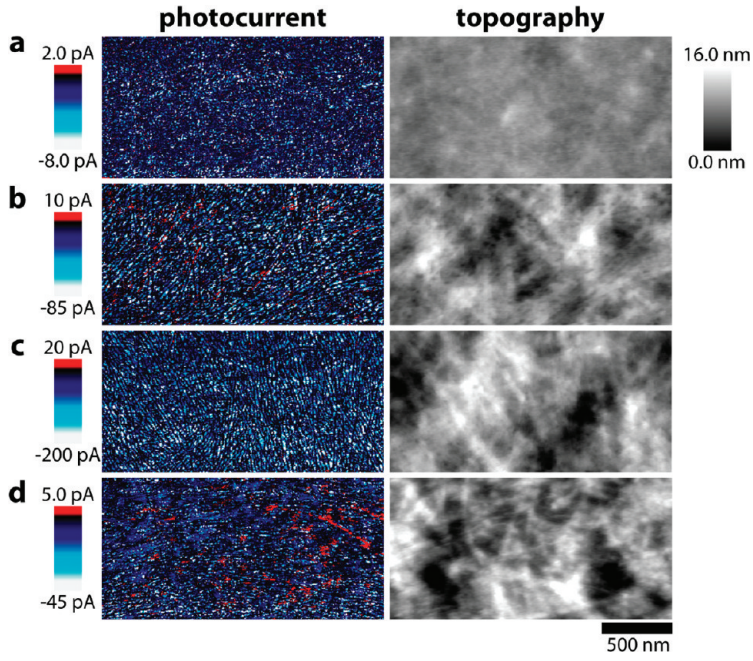

Figure 8. Photoconductive AFM images of P3BT-nw:$PC_{71}BM$ (1:1) films processed under condition A (a), condition B (b), condition C (c), and condition D (d). The tip and sample were grounded in all images.

morphology. Figure 8a−d shows a set of pc-AFM images of 1:1 P3BT-nw/$PC_{71}BM$ films prepared using the four different drying and annealing conditions, including topography (right) and photocurrent (left). We find a good qualitative correlation between the average photocurrent in each image and the short-circuit current of the corresponding devices (Supporting Information, Figure S6). Thus, we believe these images are representative of how full devices operate and can help explain our observations of the trends in V_{OC} and J_{SC} as a function of drying and annealing condition.

For the sample which was never annealed (condition D, Figure 8d), we see a very disordered structure in the photocurrent image, with some areas of the film producing positive photocurrent, and others producing negative photocurrent; nowhere is it very efficient.

At first the idea that different regions of the device produce different signs of photocurrent may appear confusing, but it ought to be expected. Because we are using a gold tip, there is little built-in field from the work-function offset of the electrodes. Thus, the sign of the photocurrent we see is solely determined by the local orientation of the donor−acceptor heterojunction if the light intensity is sufficiently high. If the surface is rich in the electron acceptor, and a good hole transport network to the substrate electrode is present, then we would expect to see a negative photocurrent; electron extraction through the tip. Conversely, if the surface is rich in the electron donor, and a good electron transport network to the substrate electrode is present, we would expect a positive photocurrent; hole collection with the tip. No matter which component of the blend is on the surface, if there is not a good transport network for the opposite carrier to the back contact, very little, if any, photocurrent will be observed. So, in Figure 6, we can assign regions of negative (blue-white) photocurrent to fullerene-rich domains, and regions of positive (red) photocurrent to P3BT-rich domains. The domains that produce no photocurrent (black) cannot be assigned without an appeal to their shape or other distinctive features. An important corollary of this statement is that high hole currents observed in cAFM images are not necessarily indicative of regions that will produce positive photocurrents. See our Supporting Information, Figure S7 for a cartoon of this interpretation.

With this interpretation in mind, it becomes clear how the disordered structure of the film in Figure 8D leads to poor device performance. Each separate domain of the device may be taken as an individual nanoscale solar cell, and the overall performance interpreted as the result of connecting them in parallel. Clearly a device containing regions which operate preferentially in opposite directions will have a detrimental effect on the short circuit current and open-circuit voltage.

In the film prepared under condition C (Figure 8c), we see a very different situation. The photocurrent image shows an ordered array of bright blue-white phases (strongly negative photocurrent) webbed with black lines. These, we take to be fullerene-rich aggregates and polymer nanowires, respectively. We have already established that the nanowires become better aligned and perhaps more uniformly horizontal in the plane of the film upon annealing, and that the fullerene aggregates between/along the nanowires. These observations are confirmed in this image. The structure in Figure 8c appears to be a nearly ideal photovoltaic morphology from the standpoint of charge generation and collection. Here we have strongly interconnected phases of the donor and acceptor, separated on a regular, periodic length scale of ~20 nm; approximately two times the exciton diffusion length.[4] Indeed the device prepared from this film structure exhibited the highest short circuit current density of the whole set (Figure 1b). Furthermore, relative to the film in Figure 8d, the sign of the photocurrent is quite consistent, with very few red spots of positive photocurrent appearing, although they are still present. Thus, we would also expect a greatly improved open-circuit voltage, relative to the film in Figure 8d. Consultation of the bulk device properties in Table 2 shows that this is indeed the case.

In the film prepared under condition B (intermediate drying time; Figure 8b), we see an increase in disorder in the photocurrent image. We have already established that annealing under this drying condition causes significant reorganization of the polymer and partial dissolution of the nanowires due to the relatively

large quantity of solvent remaining in the film. We still see the interconnected blue-white fullerene phases, but these appear both wider and shorter than in Figure 8c. In addition, the red regions of positive photocurrent have returned. There is also an increase in the background area which is simply dark, producing very little photocurrent. With fewer, shorter nanowires to guide fullerene aggregation and transport holes to the back contact, the overall efficiency is substantially reduced. From these observations we would predict a lowered open-circuit voltage, and much reduced short circuit current, which is in good agreement with the bulk results in Table 2.

In the film prepared with condition A (short drying time; Figure 8a), we see no remaining evidence of P3BT nanowires. The fullerene has formed small (~10 nm) disconnected phases on the surface of the film. There is no evidence of positive photocurrent (slight red stippling is due to system noise). The overall current is very low, with many black regions which produce almost nothing. This structure with its ~10 nm characteristic length scale can be expected to harvest excitons very efficiently. However without nanowires to guide the fullerene phase formation, and form the hole transport network, charge extraction should be poor, explaining the low total photocurrent in the devices made from this structure. Likewise the dominance of a single sign of the photocurrent and the lack of nanowires to bridge the film and create shunt paths can account for the observed increase of the open circuit voltage and fill factor.

CONCLUSIONS

We have systematically varied the nanostructure of a new type of bulk heterojunction solar cells, P3BT-nw/fullerene blend films, using a combination of thermal and solvent annealing. We used a combination of bulk device measurements and nanoscale characterization to not only describe what the changes in structure and performance are but also explain how they are connected.

The structure of the P3BT-nw/fullerene blends evolves as a function of how long the film is allowed to dry after spin coating before thermal annealing. At short drying times, the film still contains residual solvent, which dissolves the polymer nanowires, so varying the drying time adjusts the density of nanowires in the film after annealing. Films that are allowed to dry completely before annealing show very little change in the nanowires structure, but the fullerene phase evolves significantly, aggregating in the interstices of the nanowire structure. Pure P3BT-nw films that are annealed after a short drying time form a bulk crystal phase of P3BT as the nanowires dissolve. However, this process is inhibited in the blended films. Figure 9 shows a cartoon of our proposed structural evolution.

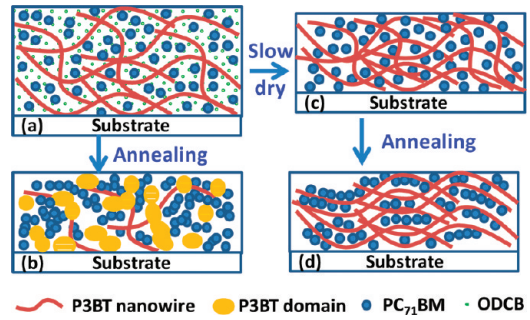

Figure 9. Illustration of P3BT-nw:$PC_{71}BM$ blend film drying process.

Contrary to traditional wisdom, we found that the devices with the highest bulk SCLC hole mobility also had the lowest photovoltaic performance. Our cAFM and pcAFM experiments explain this observation, showing that when nanowires bridge the device it is beneficial for hole mobility, but not photovoltaic performance. This result highlights the need for truly nanoscale modeling and measurements in order to accurately characterize the behavior of organic photovoltaic devices.

We found that a high density of nanowires, combined with an ordered fullerene phase aggregated in the interstices of the nanowire structure, was ideal for the quantum efficiency of the device. The nanowires provide an efficient hole transport network and guide the PCBM phases into a mirroring electron transport network. However, the long P3BT nanowires bridge the device and reduce the open circuit voltage and fill factor. The open circuit voltage and fill factor were maximized in devices containing no nanowires, but the current densities were significantly lower. The optimal average power conversion efficiency was found in a device structure which balanced these characteristics. Thus, we believe that at short aging times the primary loss mechanism is related to inefficient charge collection, while at long aging times the primary loss mechanism appears to be shunt pathways produced by the nanowires. We believe that polymer nanowire/fullerene composites have the potential for significantly higher power conversion efficiency in a structure that retains the ideal interpenetrating heterojunction of polymer nanowires and fullerene phases while avoiding the device bridging effect of the nanowires.

EXPERIMENTAL SECTION

Materials. Poly(3-butylthiophene) (P3BT, 97% head-to-tail regioregularity) was purchased from Aldrich. The weight-average molecular weight (M_w) and polydispersity index of this P3BT sample measured in our lab are 21 500 and 2.22, respectively. The fullerene, [6,6]-phenyl-C_{71}-butyric acid methyl ester ($PC_{71}BM$, > 99.5%), was obtained from American Dye Source, Inc. (Quebec, Canada). All the chemicals were used as received without

further purification. Poly(3,4-ethylenedioxythiophene):poly(styrene sulfonate) (PEDOT) (Baytron P VP AI 4083) was purchased from H. C. Stark (Newton, MA) and passed through a 0.45 μm PVDF filter before spin-coating.

Preparation of P3BT Nanowires. A 3 mL aliquot of nitrogen-degassed 1,2-dichlorobenzene (ODCB) solvent was added to a 10 mL bottle containing 24 mg of P3BT sample; the suspension (8 mg/mL) was stirred for 5 h at 90−100 °C until P3BT was completely dissolved. The hot solution was filtered through a 0.45 μm PTFE membrane, and the filtrate was put in a dark environment for 72 h to allow P3BT molecules to self-assemble. The original orange brown color of the solution changed to dark brown after the P3BT nanowires (P3BT-nw) were formed as a dispersion. The P3BT nanowire suspension was found to be quite stable. The nanowires did not dissolve in ODCB when diluted and did not precipitate over more than a three month period.

Fabrication and Testing of Solar Cells. The $PC_{71}BM$ solution was prepared by dissolving 60 mg $PC_{71}BM$ in 1 mL of nitrogen-degassed ODCB, and the solution (60 mg/mL) was stirred at 40 °C overnight and passed through a 0.2 μm PTFE filter. The P3BT-nw:$PC_{71}BM$ blends were made by mixing the P3BT-nw suspension with $PC_{71}BM$ solution at different ratios and stirring the mixture for 20 min before spin-coating.

Solar cells were fabricated by first spin-coating a PEDOT buffer layer on top of ITO-coated glass substrates (10 Ω/□, Shanghai B. Tree Tech. Consult Co., Ltd., Shanghai, China) at 3500 rpm for 40 s and then drying at 150 °C for 10 min under vacuum. The thickness of PEDOT was around 40 nm. The active blend layer was spin-coated on top of the PEDOT layer from the P3BT-nw:$PC_{71}BM$ blend at a speed of 1000 rpm for 30 s in a glovebox, and substrate was immediately transferred to a covered Petri dish for drying. After a measured drying time, the film was either annealed on a 170 ± 10 °C hot plate for 10 min first or directly taken out of the glovebox and loaded in a thermal evaporator (BOC Edwards, 306) for the deposition of the cathode. The active layer had a thickness of about 80 nm. The cathode, consisting of 1.0 nm LiF and 80 nm aluminum layers, was sequentially deposited through a shadow mask on top of the active layer in a vacuum of 8×10^{-7} Torr. Each substrate contained five solar cells with an active area of 3.57 mm^2. Photovoltaic cells with a structure of ITO/PEDOT/P3BT-nw: $PC_{71}BM$/LiF/Al were tested under a 100 mW/cm^2 AM1.5 simulated sunlight in ambient air.

Measurement of Charge-Carrier Mobility. Devices for SCLC hole mobility measurement were fabricated in an identical manner, except that a gold electrode was deposited instead of the lithium fluoride (LiF) and aluminum cathode used in the solar cells to facilitate hole-only transport. Film thicknesses were measured with an Alpha-Step 500 profilometer (KLA-Tencor, San Jose, CA). Current−voltage characteristics of both solar cells and SCLC devices were measured using a HP4155A semiconductor parameter analyzer (Yokogawa Hewlett-Packard, Tokyo). The light intensity of 1.5 a.m. sunlight from a filtered Xe lamp was controlled by using a set of neutral density filters. The SCLC characteristics were measured under dark conditions. All the bulk device characterization steps were carried out under ambient laboratory air.

Field-effect transistors were fabricated on heavily doped (n-type) silicon substrates with thermally grown silicon dioxide (300 nm). Doped silicon acted as a common gate electrode, and silicon dioxide acted as the gate insulator. Source and drain electrodes were patterned on top of the substrates using photolithography and thermal evaporation of 2 nm thick chromium and 60 nm thick gold layers. The bottom-contact/bottom-gate devices had a channel width of 800 μm and length of 20 μm. Substrates were cleaned by ultrasonication in sequential acetone and isopropyl alcohol baths, purged with argon. An octyltriethoxysilane (OTS-8) monolayer was vapor deposited on the substrates in a vacuum desiccator at 60 °C for more than 6 h and cross-linked by placing the monolayer/substrate on a hot plate at 120 °C for 20 min. The nanowire suspension and nanowires/fullerene blends with different compositions were spin-coated on the substrates (2000 rpm, 60 s). Devices were processed under the same conditions as described above for solar cells. Electrical characteristics of the field-effect transistors were measured on a Keithley 4200 semiconductor characterization system (Keithley Instruments Inc. Cleveland, OH). The field-effect mobility was calculated from the equation for the saturation region, following our previous reported approaches.[55,56] All the bulk measurements were done under dark conditions in air.

Imaging. The AFM topography images were acquired with a Dimension 3100 Scanning Probe Microscope (Veeco Instruments Inc., Woodbury, NY) in tapping mode. The films for atomic force microscopy (AFM) imaging of surface morphology were prepared in a manner identical to those for device measurements.

The conductive and photoconductive AFM images were acquired with an MFP-3D atomic force microscope (Asylum Research, Santa Barbara, CA) using an ORCA-2 current preamplifier and a nitrogen flow cell. All current measurements were performed using gold-coated Si cantilevers from Budget Sensors (Cont-GB, $k = 0.2$ N/m). The pc-AFM experimental setup is described in detail elsewhere.[46,48,49] Briefly, we mount the AFM on an inverted optical microscope (Nikon, Eclipse T2000-U.) and focus a 532 nm laser to a diffraction limited spot centered on the AFM tip. Light intensity is controlled *via* neutral density filters. The AFM tip forms the top contact of a nanoscale solar cell, which we use to simultaneously map the short-circuit photocurrent and topography with ~25 nm resolution. Samples were mounted in ambient laboratory air, but care was taken to minimize light exposure and air exposure time. The flow cell was allowed to purge for at least 30 min before imaging or laser illumination.

Bright-field transmission electron images (BF-TEM) were measured on an FEI Tecnai G^2 F20 TEM at 200 kV accelerating voltage. The images were slightly defocused to enhance the phase contrast and were then acquired with a CCD camera and recorded with Gatan DigitalMicrograph software with proper exposure time.

Absorption Spectroscopy. UV−vis absorption spectra were recorded on a Perkin-Elmer model Lambda 900 UV−vis−near-IR spectrophotometer. Both P3BT-nw and P3BT-nw:$PC_{71}BM$ blend films for absorption measurements were spin-coated on top of ITO/PEDOT substrates and measured by using ITO/PEDOT substrate as reference.

Acknowledgment. This report is based on work (Polymer and Hybrid Organic/Inorganic Solar Cells) supported by the US Department of Energy, Office of Basic Energy Sciences, Division of Materials Sciences under Award No. DE-FG02-07ER46467. S.A.J. acknowledges the NSF (DMR-0805259 and DMR-0120967) for the initial synthesis of polymer nanowires. D.S.G. acknowledges the NSF (DMR-0120967 and DMR-0449422) for supporting the initial development of the tools that made this study possible. O.G.R. acknowledges partial support from an IGERT Fellowship Award under NSF No. DGE-0504573 at the Center for Nanotechnology at the UW. G.R. acknowledges the University of Washington Initiatives Fund (UIF) fellowship from the Center for Nanotechnology. Part of this work was conducted at the University of Washington NanoTech User Facility, a member of the NSF National Nanotechnology Infrastructure Network (NNIN).

Supporting Information Available: UV−vis absorption spectra, EQE spectra, *J*−*V* curves of space−charge limited current, X-ray diffraction spectra, OFET transfer characteristics, photocurrent obtained from pc-AFM imaging. This material is available free of charge *via* the Internet at http://pubs.acs.org.

REFERENCES AND NOTES

1. Coakley, K. M.; McGehee, M. D. Conjugated Polymer Photovoltaic Cells. *Chem. Mater.* **2004**, *16*, 4533–4542.
2. Blom, P. W. M.; Mihailetchi, V. D.; Koster, L. J. A.; Markov, D. E. Device Physics of Polymer: Fullerene Bulk Heterojunction Solar Cells. *Adv. Mater.* **2007**, *19*, 1551–1566.
3. Thompson, B. C.; Frechet, J. M. J. Organic Photovoltaics—Polymer−Fullerene Composite Solar Cells. *Angew. Chem., Int. Ed.* **2008**, *47*, 58–77.
4. Gunes, S.; Neugebauer, H.; Sariciftci, N. S. Conjugated Polymer-Based Organic Solar Cells. *Chem. Rev.* **2007**, *107*, 1324–1338.

5. Nguyen, L. H.; Hoppe, H.; Erb, T.; Gunes, S.; Gobsch, G.; Sariciftci, N. S. Effects of Annealing on the Nanomorphology and Performance of Poly(alkylthiophene): Fullerene Bulk-Heterojunction Solar Cells. *Adv. Funct. Mater.* **2007**, *17*, 1071–1078.
6. Chen, L. M.; Hong, Z. R.; Li, G.; Yang, Y. Recent Progress in Polymer Solar Cells: Manipulation of Polymer: Fullerene Morphology and the Formation of Efficient Inverted Polymer Solar Cells. *Adv. Mater.* **2009**, *21*, 1434–1449.
7. Li, G.; Shrotriya, V.; Huang, J. S.; Yao, Y.; Moriarty, T.; Emery, K.; Yang, Y. High-Efficiency Solution Processable Polymer Photovoltaic Cells by Self-Organization of Polymer Blends. *Nat. Mater.* **2005**, *4*, 864–868.
8. Ma, W. L.; Yang, C. Y.; Gong, X.; Lee, K.; Heeger, A. J. Thermally Stable, Efficient Polymer Solar Cells with Nanoscale Control of the Interpenetrating Network Morphology. *Adv. Funct. Mater.* **2005**, *15*, 1617–1622.
9. Woo, C. H.; Thompson, B. C.; Kim, B. J.; Toney, M. F.; Frechet, M. J. The Influence of Poly(3-hexylthiophene) Regioreigularity on Fullerene-Composite Solar Cell Performance. *J. Am. Chem. Soc.* **2008**, *130*, 16324–16329.
10. Kim, Y.; Cook, S.; Tuladhar, S. M.; Choulis, S. A.; Nelson, J.; Durrant, J. R.; Bradley, D. D. C.; Giles, M.; McCulloch, I.; Ha, C. S.; *et al.* A Strong Regioregularity Effect in Self-Organizing Conjugated Polymer Films and High-Efficiency Polythiophene: Fullerene Solar Cells. *Nat. Mater.* **2006**, *5*, 197–203.
11. Kim, J. Y.; Lee, K.; Coates, N. E.; Moses, D.; Nguyen, T. Q.; Dante, M.; Heeger, A. J. Efficient Tandem Polymer Solar Cells Fabricated by All-Solution Processing. *Science* **2007**, *317*, 222–225.
12. Muhlbacher, D.; Scharber, M.; Morana, M.; Zhu, Z. G.; Waller, D.; Gaudiana, R.; Brabec, C. High Photovoltaic Performance of a Low-Bandgap Polymer. *Adv. Mater.* **2006**, *18*, 2884–2889.
13. Thompson, B. C.; Kim, Y. G.; McCarley, T. D.; Reynolds, J. R. Soluble Narrow Band Gap and Blue Propylenedioxythiophene−Cyanovinylene Polymers as Multifunctional Materials for Photovoltaic and Electrochromic Applications. *J. Am. Chem. Soc.* **2006**, *128*, 12714–12725.
14. Wong, W. Y.; Wang, X. Z.; He, Z.; Chan, K. K.; Djurisic, A. B.; Cheung, K. Y.; Yip, C. T.; Ng, A. M. C.; Xi, Y. Y.; Mak, C. S. K.; *et al.* Tuning the Absorption, Charge Transport Properties, and Solar Cell Efficiency with the Number of Thienyl Rings in Platinum-Containing Poly(aryleneethynylene)s. *J. Am. Chem. Soc.* **2007**, *129*, 14372–14380.
15. Blouin, N.; Michaud, A.; Gendron, D.; Wakim, S.; Blair, E.; Neagu-Plesu, R.; Belletete, M.; Durocher, G.; Tao, Y.; Leclerc, M. Toward a Rational Design of Poly(2,7-carbazole) Derivatives for Solar Cells. *J. Am. Chem. Soc.* **2008**, *130*, 732–742.
16. Chen, C. P.; Chan, S. H.; Chao, T. C.; Ting, C.; Ko, B. T. Low-Bandgap Poly(thiophene-phenylene-thiophene) Derivatives with Broaden Absorption Spectra for Use in High-Performance Bulk-Heterojunction Polymer Solar Cells. *J. Am. Chem. Soc.* **2008**, *130*, 12828–12833.
17. Hou, J. H.; Chen, H. Y.; Zhang, S. Q.; Li, G.; Yang, Y. Synthesis, Characterization, and Photovoltaic Properties of a Low Band Gap Polymer Based on Silole-Containing Polythiophenes and 2,1,3-Benzothiadiazole. *J. Am. Chem. Soc.* **2008**, *130*, 16144–16145.
18. Wang, E. G.; Wang, L.; Lan, L. F.; Luo, C.; Zhuang, W. L.; Peng, J. B.; Cao, Y. High-Performance Polymer Heterojunction Solar Cells of a Polysilafluorene Derivative. *Appl. Phys. Lett.* **2008**, *92*, 033307.
19. Wienk, M. M.; Turbiez, M.; Gilot, J.; Janssen, R. A. J. Narrow-Bandgap Diketo-Pyrrolo-Pyrrole Polymer Solar Cells: The Effect of Processing on the Performance. *Adv. Mater.* **2008**, *20*, 2556–2560.
20. Liang, Y. Y.; Feng, D. Q.; Wu, Y.; Tsai, S. T.; Li, G.; Ray, C.; Yu, L. P. Highly Efficient Solar Cell Polymers Developed *via* Fine-Tuning of Structural and Electronic Properties. *J. Am. Chem. Soc.* **2009**, *131*, 7792–7799.
21. Park, S. H.; Roy, A.; Beaupre, S.; Cho, S.; Coates, N.; Moon, J. S.; Moses, D.; Leclerc, M.; Lee, K.; Heeger, A. J. Bulk Heterojunction Solar Cells with Internal Quantum Efficiency Approaching 100%. *Nat. Photonics* **2009**, *3*, 297–302.
22. Wu, P.-T.; Bull, T.; Kim, F. S.; Luscombe, C. K.; Jenekhe, S. A. Organometallic Donor−Acceptor Conjugated Polymer Semiconductors: Tunable Optical, Electrochemical, Charge Transport, and Photovoltaic Properties. *Macromolecules* **2009**, *42*, 671–681.
23. Wu, P.-T.; Ren, G. Q.; Li, C. X.; Mezzenga, R.; Jenekhe, S. A. Crystalline Diblock Conjugated Copolymers: Synthesis, Self-Assembly, and Microphase Separation of Poly(3-butylthiophene)-*b*-poly(3-octylthiophene). *Macromolecules* **2009**, *42*, 2317–2320.
24. Bull, T. A.; Pingree, L. S. C.; Jenekhe, S. A.; Ginger, D. S.; Luscombe, C. K. The Role of Mesoscopic PCBM Crystallites in Solvent Vapor Annealed Copolymer Solar Cells. *ACS Nano* **2009**, *3*, 627–636.
25. Xin, H.; Guo, X. G.; Kim, F. S.; Ren, G. Q.; Watson, M. D.; Jenekhe, S. A. Efficient Solar Cells Based on a New Phthalimide-Based Donor-Acceptor Copolymer Semiconductor: Morphology, Charge-Transport, and Photovoltaic Properties. *J. Mater. Chem.* **2009**, *19*, 5303–5310.
26. Peet, J.; Kim, J. Y.; Coates, N. E.; Ma, W. L.; Moses, D.; Heeger, A. J.; Bazan, G. C. Efficiency Enhancement in Low-Bandgap Polymer Solar Cells by Processing with Alkane Dithiols. *Nat. Mater.* **2007**, *6*, 497–500.
27. Shrotriya, V.; Yao, Y.; Li, G.; Yang, Y. Effect of Self-Organization in Polymer/Fullerene Bulk Heterojunctions on Solar Cell Performance. *Appl. Phys. Lett.* **2006**, *89*, 063505.
28. Li, G.; Yao, Y.; Yang, H.; Shrotriya, V.; Yang, G.; Yang, Y. "Solvent Annealing" Effect in Polymer Solar Cells Based on Poly(3-hexylthiophene) and Methanofullerenes. *Adv. Funct. Mater.* **2007**, *17*, 1636–1644.
29. Gledhill, S. E.; Scott, B.; Gregg, B. A. Organic and Nanostructured Composite Photovoltaics: An Overview. *J. Mater. Res.* **2005**, *20*, 3167–3179.
30. Padinger, F.; Rittberger, R. S.; Sariciftci, N. S. Effects of Postproduction Treatment on Plastic Solar Cells. *Adv. Funct. Mater.* **2003**, *13*, 85–88.
31. Zhao, Y.; Xie, Z. Y.; Qu, Y.; Geng, Y. H.; Wang, L. X. Solvent-Vapor Treatment Induced Performance Enhancement of Poly(3-hexylthiophene): Methanofullerene Bulk-Heterojunction Photovoltaic Cells. *Appl. Phys. Lett.* **2007**, *90*, 043504.
32. Berson, S.; De Bettignies, R.; Bailly, S.; Guillerez, S. Poly(3-hexylthiophene) Fibers for Photovoltaic Applications. *Adv. Funct. Mater.* **2007**, *17*, 1377–1384.
33. Yang, X. N.; Loos, J.; Veenstra, S. C.; Verhees, W. J. H.; Wienk, M. M.; Kroon, J. M.; Michels, M. A. J.; Janssen, R. A. J. Nanoscale Morphology of High-Performance Polymer Solar Cells. *Nano Lett.* **2005**, *5*, 579–583.
34. Campbell, A. R.; Hodgkiss, J. M.; Westenhoff, S.; Howard, I. A.; Marsh, R. A.; McNeill, C. R.; Friend, R. H.; Greenham, N. C. Low-Temperature Control of Nanoscale Morphology for High Performance Polymer Photovoltaics. *Nano Lett.* **2008**, *8*, 3942–3947.
35. Lee, J. K.; Ma, W. L.; Brabec, C. J.; Yuen, J.; Moon, J. S.; Kim, J. Y.; Lee, K.; Bazan, G. C.; Heeger, A. J. Processing Additives for Improved Efficiency from Bulk Heterojunction Solar Cells. *J. Am. Chem. Soc.* **2008**, *130*, 3619–3623.
36. Moule, A. J.; Meerholz, K. Controlling Morphology in Polymer−Fullerene Mixtures. *Adv. Mater.* **2008**, *20*, 240–245.
37. Pivrikas, A.; Stadler, P.; Neugebauer, H.; Sariciftci, N. S. Substituting the Postproduction Treatment for Bulk-Heterojunction Solar Cells Using Chemical Additives. *Org. Electron.* **2008**, *9*, 775–782.
38. van Bavel, S. S.; Sourty, E.; de With, G.; Loos, J. Three-Dimensional Nanoscale Organization of Bulk Heterojunction Polymer Solar Cells. *Nano Lett.* **2009**, *9*, 507–513.
39. Miller, S.; Fanchini, G.; Lin, Y. Y.; Li, C.; Chen, C. W.; Su, W. F.;

Chhowalla, M. Investigation of Nanoscale Morphological Changes in Organic Photovoltaics During Solvent Vapor Annealing. *J. Mater. Chem.* **2008**, *18*, 306–312.
40. Dante, M.; Garcia, A.; Nguyen, T. Q. Three-Dimensional Nanoscale Organization of Highly Efficient Low Band-Gap Conjugated Polymer Bulk Heterojunction Solar Cells. *J. Phys. Chem. C* **2009**, *113*, 1596–1600.
41. Yao, Y.; Hou, J. H.; Xu, Z.; Li, G.; Yang, Y. Effect of Solvent Mixture on the Nanoscale Phase Separation in Polymer Solar Cells. *Adv. Funct. Mater.* **2008**, *18*, 1783–1789.
42. Coates, N. E.; Hwang, I. W.; Peet, J.; Bazan, G. C.; Moses, D.; Heeger, A. J. 1,8-Octanedithiol as a Processing Additive for Bulk Heterojunction Materials: Enhanced Photoconductive Response. *Appl. Phys. Lett.* **2008**, *93*, 072105.
43. Xin, H.; Kim, F. S.; Jenekhe, S. A. Highly Efficient Solar Cells Based on Poly(3-butylthiophene) Nanowires. *J. Am. Chem. Soc.* **2008**, *130*, 5424–5425.
44. Xin, H.; Ren, G. Q.; Kim, F. S.; Jenekhe, S. A. Bulk Heterojunction Solar Cells from Poly(3-butylthiophene)/Fullerene Blends: *In Situ* Self-Assembly of Nanowires, Morphology, Charge Transport, and Photovoltaic Properties. *Chem. Mater.* **2008**, *20*, 6199–6207.
45. Hiorns, R. C.; De Bettignies, R.; Leroy, J.; Bailly, S.; Firon, M.; Sentein, C.; Khoukh, A.; Preud'homme, H.; Dagron-Lartigau, C. High Molecular Weights, Polydispersities, and Annealing Temperatures in the Optimization of Bulk-Heterojunction Photovoltaic Cells Based on Poly(3-hexylthiophene) or Poly(3-butylthiophene). *Adv. Funct. Mater.* **2006**, *16*, 2263–2273.
46. Coffey, D. C.; Reid, O. G.; Rodovsky, D. B.; Bartholomew, G. P.; Ginger, D. S. Mapping Local Photocurrents in Polymer/Fullerene Solar Cells with Photoconductive Atomic Force Microscopy. *Nano Lett.* **2007**, *7*, 738–744.
47. Reid, O. G.; Munechika, K.; Ginger, D. S. Space Charge Limited Current Measurements on Conjugated Polymer Films Using Conductive Atomic Force Microscopy. *Nano Lett.* **2008**, *8*, 1602–1609.
48. Pingree, L. S. C.; Reid, O. G.; Ginger, D. S. Electrical Scanning Probe Microscopy on Active Organic Electronic Devices. *Adv. Mater.* **2009**, *21*, 19–28.
49. Pingree, L. S. C.; Reid, O. G.; Ginger, D. S. Imaging the Evolution of Nanoscale Photocurrent Collection and Transport Networks during Annealing of Polythiophene/Fullerene Solar Cells. *Nano Lett.* **2009**, *9*, 2946–2952.
50. Moliton, A.; Nunzi, J. M. How to Model the Behaviour of Organic Photovoltaic Cells. *Polym. Int.* **2006**, *55*, 583–600.
51. Cascio, A. J.; Lyon, J. E.; Beerbom, M. M.; Schlaf, R.; Zhu, Y.; Jenekhe, S. A. Investigation of a Polythiophene Interface Using Photoemission Spectroscopy in Combination with Electrospray Thin-Film Deposition. *Appl. Phys. Lett.* **2006**, *88*, 062104.
52. Chen, T. A.; Wu, X. M.; Rieke, R. D. Regiocontrolled Synthesis of Poly(3-alkylthiophenes) Mediated by Rieke Zinc—Their Characterization and Solid-State Properties. *J. Am. Chem. Soc.* **1995**, *117*, 233–244.
53. Causin, V.; Marega, C.; Marigo, A.; Valentini, L.; Kenny, J. M. Crystallization and Melting Behavior of Poly(3-butylthiophene), Poly(3-octylthiophene), and Poly(3-dodecylthiophene). *Macromolecules* **2005**, *38*, 409–415.
54. Hoppe, H.; Niggemann, M.; Winder, C.; Kraut, J.; Hiesgen, R.; Hinsch, A.; Meissner, D.; Sariciftci, N. S. Nanoscale Morphology of Conjugated Polymer/Fullerene-Based Bulk-Heterojunction Solar Cells. *Adv. Funct. Mater.* **2004**, *14*, 1005–1011.
55. Babel, A.; Wind, J. D.; Jenekhe, S. A. Ambipolar Charge Transport in Air-Stable Polymer Blend Thin-Film Transistors. *Adv. Funct. Mater.* **2004**, *14*, 891–898.
56. Zhu, Y.; Champion, R. D.; Jenekhe, S. A. Conjugated Donor−Acceptor Copolymer Semiconductors with Large Intramolecular Charge Transfer: Synthesis, Optical Properties, Electrochemistry, and Field Effect Carrier Mobility of Thienopyrazine-Based Copolymers. *Macromolecules* **2006**, *39*, 8712–8719.